Measuring deviations from the Kerr geometry with black hole ringdown

Kallol Dey,[1] Enrico Barausse,[2,3] and Soumen Basak[1]

[1]*School of Physics, Indian Institute of Science Education and Research Thiruvananthapuram, Maruthamala PO, Vithura, Thiruvananthapuram 695551, Kerala, India*

[2]*SISSA, Via Bonomea 265, 34136 Trieste, Italy and Istituto Nazionale di Fisica Nucleare (INFN)—Sezione di Trieste, Trieste, Italy*

[3]*IFPU—Institute for Fundamental Physics of the Universe, Via Beirut 2, 34014 Trieste, Italy*

(Received 23 December 2022; accepted 12 July 2023; published 28 July 2023)

Black holes in general relativity are famously characterized by two "hairs" only, the mass and the spin of the Kerr spacetime. Theories extending general relativity, however, allow in principle for additional black hole charges, which will generally modify the multipole structure of the Kerr solution. Here, we show that gravitational wave observations of the postmerger ringdown signal from black hole binaries may permit measuring these additional hairs. We do so by considering spacetime geometries differing from the Kerr one at the level of the quadrupole moment, and computing the differences of their quasinormal mode frequencies from the Kerr ones in the eikonal limit. We then perform a Bayesian analysis with current and future gravitational wave data and compute posterior constraints for the quadrupole deviation away from Kerr. We find that the inclusion of higher modes, which are potentially observable by future detectors, will allow for constraining deviations from the Kerr quadrupole at percent level.

DOI: 10.1103/PhysRevD.108.024064

I. INTRODUCTION

The most generic stationary and asymptotically flat black hole (BH) spacetimes of general relativity (GR) are given by the Kerr-Newman solution [1–4], which is characterized by three parameters (mass, spin and electric charge). Since the electric charge is currently believed to be astrophysically unimportant [5], astrophysical BHs are expected to possess only two charges (or "hairs"), i.e. the mass and the spin. This is usually referred to as the "no-hair theorem" of GR. Theories extending GR, however, may allow for BHs different from the Kerr (or Kerr-Newman) geometry [6]. These BH spacetimes will generally present additional hairs, see e.g. [7] for a review. As a result, they will present a multipole structure different from that of Kerr BHs, from which they may deviate already at the quadrupole order (or higher).

Gravitational wave (GW) observations of extreme mass-ratio inspirals have long been understood to hold the potential to test these putative deviations from Kerr [8,9], with projected bounds on the quadrupole deviation with the Laser Interferometer Space Antenna (LISA) [10] reaching a fractional order of 10^{-5} [11]. Similar constraints on deviations from Kerr can also be obtained with x-ray observations of accretion disks around BHs (either ones of the continuum spectrum [12,13] or fluorescent iron lines [14,15]) or, more recently, with the Event Horizon Telescope [16,17]. Moreover, with the growing number of GW signals detected by the LIGO-Virgo-KAGRA (LVK) collaboration [18–26], attempts have also been made at exploiting the inspiral phase of stellar-origin BH binaries for similar tests of the no-hair theorem [27–32].

Tests of GR with the postmerger ringdown signal, known as "BH spectroscopy," also have a long history, dating back to [33–35]. These tests hinge on the fact that within GR the (complex) quasinormal mode (QNM) frequencies are only a function of mass and spin (again due to the no-hair theorem), a hypothesis that can be tested by measuring two independent modes. The LVK detections are so far in agreement with the QNM ringdown frequencies predicted by GR, with evidence for the presence of the dominant $\ell = m = 2$, $n = 0$ mode (in GW150914) and possibly[1] also the $\ell = m = 3$, $n = 0$ (in GW190521) and $\ell = m = 2$, $n = 1$ (in GW150914) modes. However, tests of GR with QNMs require higher signal-to-noise ratio, which will only be possible with next generation detectors [43–46]. In the meantime, much work has already gone into developing theory agnostic parametrizations of the deviations of the ringdown signal from the GR prediction [47–55].

In this paper, we will study what constraints on the deviation of the quadrupole moment away from the Kerr spacetime's value can be obtained from the ringdown signal

[1]These claims have been shown to depend on the characterization of the detector noise, the data analysis methods, the choice of starting time for the ringdown phase, and even nonlinear effects in the ringdown modeling [36–42].

of the GW150914 event. We will also show how these constraints will improve with next-generation detectors such as the Einstein Telescope. In order to describe the non-Kerr BH spacetime, we will utilize two metric *ansatze* commonly employed in the literature on tests of the quadrupole moment of the Kerr metric, i.e. the Manko-Novikov (MN) metric [56] and the Johannsen-Psaltis (JP) metric [57].

The former is a vacuum stationary and axisymmetric solution of the Einstein equations of GR, which can describe the exterior of a rotating star or exotic compact object (see e.g. [58]), but which is also defined in the strong field region. In that regime, however, pathologies necessarily appear (because of the no-hair theorem of GR), i.e. the spacetime presents a partial event horizon with a curvature singularity on the equatorial plane, as well as closed timelike curves. These pathologies are "covered" by the star's or exotic compact object's matter if the metric describes one such body. The MN metric allows for deviations from the Kerr geometry at any multipole order, but in this work we will only study quadrupole deviations. The JP metric, instead, is not a solution of the GR field equations nor of those of any extensions of GR. It is a purely phenomenological parametrization of possible deviations from the Kerr hypothesis (see also [59–63] for a similar metric *ansatz*), and it has been widely used for tests of the no-hair theorem with electromagnetic observations [64–67].

Starting from either of these two geometries, we compute the deviations of the QNM frequencies of the dominant $\ell = m = 2$, $n = 0$ mode from the Kerr values, in the eikonal (i.e. geometric optics) approximation. Although this approximation is formally only valid in the limit of large ℓ, it has been shown to approximately describe also the low-ℓ modes in GR, and it has also been applied beyond GR [29,68,69].

We then use Bayesian methods to obtain posterior constraints on the quadrupole moment's deviation from Kerr, using existing ringdown data (GW150914) and future simulated ones [assuming detections by the Einstein Telescope (ET)]. We find that the posteriors for the quadrupole deviation obtained from GW150914 are consistent with Kerr. Similar systems detected by ET will allow us to further improve this constraint, and break parameter degeneracies that appear between the remnant mass, spin and the quadrupole deviation.

This paper is organized as follows: In Sec. II, we discuss the MN and the JP metric *ansatze*. In Sec. III we describe the eikonal approximation technique for the calculation of QNMs. The analysis techniques adopted in this paper are introduced in Sec. IV, followed by a discussion of the results in Sec. V. We explore how future detectors might effect this analysis in Sec. VI.

II. QUADRUPOLE DEVIATION FROM KERR

In the most general case, the gravitational field around a GR compact object can be described by a stationary, axisymmetric and asymptotically flat vacuum spacetime. The corresponding metric can be expressed in terms of the Geroch-Hansen moments [70,71] M_ℓ, S_ℓ, where M_ℓ and S_ℓ are respectively the mass and current moments. It can be shown that the nonzero mass moments are respectively the mass $M_0 = M$, the mass quadrupole $M_2 = Q$, and higher order even moments, and the nonzero current moments are the angular momentum $S_1 = J$, S_3 and higher order odd moments. In the case of a Kerr spacetime, the following relation connects M_ℓ and S_ℓ:

$$M_\ell + iS_\ell = M\left(i\frac{J}{M}\right)^\ell. \tag{1}$$

This is the celebrated no-hair theorem. However, if the compact object is not a Kerr BH, Eq. (1) may not hold true and the quadrupole moment Q may deviate from its expected Kerr value of $-a^2M$. In this paper, we consider two geometries (the MN and JP ones) that describe compact objects with quadrupole moments different from Kerr.

A. Manko Novikov spacetime

The MN metric [56] describes a stationary, axisymmetric and asymptotically flat vacuum solution of Einstein's equations with arbitrary mass multipoles moments. In its full form, it has an infinite number of free parameters, but it can also reduce to the Kerr metric under appropriate conditions. The MN metric can be written in prolate spheroidal coordinates as [12,13]

$$ds^2 = -f(dt - \omega d\phi)^2 + \frac{k^2e^{2\gamma}}{f}(x^2 - y^2)\left(\frac{dx^2}{x^2-1} + \frac{dy^2}{1-y^2}\right) + \frac{k^2}{f}(x^2-1)(1-y^2)d\phi^2, \tag{2}$$

where

$$f = e^{2\psi}\frac{A}{B}, \qquad \omega = 2ke^{-2\psi}\frac{C}{A} - \frac{4k\alpha}{1-\alpha^2}, \qquad e^{2\gamma} = e^{2\gamma'}\frac{A}{(x^2-1)(1-\alpha^2)^2}, \qquad \psi = \sum_{n=1}^{+\infty}\frac{\alpha_n P_n}{R^{n+1}}, \tag{3}$$

$$\gamma' = \frac{1}{2}\log\frac{x^2-1}{x^2-y^2} + \sum_{m,n=1}^{+\infty}\frac{(m+1)(n+1)\alpha_m\alpha_n}{(m+n+2)R^{m+n+2}}(P_{m+1}P_{n+1} - P_m P_n) + \sum_{n=1}^{+\infty}\alpha_n\left((-1)^{n+1} - 1 + \sum_{k=0}^{n}\frac{x-y+(-1)^{n-k}(x+y)}{R^{k+1}}P_k\right), \tag{4a}$$

$$A = (x^2-1)(1+\tilde{a}\,\tilde{b})^2 - (1-y^2)(\tilde{b}-\tilde{a})^2, \tag{4b}$$

$$B = \{x+1+(x-1)\tilde{a}\,\tilde{b}\}^2 + \{(1+y)\tilde{a} + (1-y)\tilde{b}\}^2, \tag{4c}$$

$$C = (x^2-1)(1+\tilde{a}\,\tilde{b})\{\tilde{b}-\tilde{a}-y(\tilde{a}+\tilde{b})\} + (1-y^2)(\tilde{b}-\tilde{a})\{1+\tilde{a}\,\tilde{b}+x(1-\tilde{a}\,\tilde{b})\}, \tag{4d}$$

$$\tilde{a} = -\alpha\exp\left[\sum_{n=1}^{+\infty}2\alpha_n\left(1-\sum_{k=0}^{n}\frac{x-y}{R^{k+1}P_k}\right)\right], \tag{4e}$$

$$\tilde{b} = \alpha\exp\left[\sum_{n=1}^{+\infty}2\alpha_n\left((-1)^n + \sum_{k=0}^{n}\frac{(-1)^{n-k+1}(x+y)}{R^{k+1}}P_k\right)\right], \tag{4f}$$

where $R = \sqrt{x^2+y^2-1}$ and P_n are Legendre polynomials such that

$$P_n = P_n\left(\frac{xy}{R}\right), \tag{5}$$

$$P_n(\zeta) = \frac{1}{2^n n!}\frac{d^n}{d\zeta^n}(\zeta^2-1)^n. \tag{6}$$

These can also be expressed in Boyer-Lindquist coordinates (r,θ) using

$$r = kx + M, \qquad \cos\theta = y. \tag{7}$$

We note that the metric used in this paper is the same as in [12], which fixed some typos in the original MN metric [56]. Here, k is related to the mass of the spacetime, α to the spin and α_n to the mass multipole moments, indexed by $n=1$ (dipole), $n=2$ (quadrupole), and so on. The MN metric reduces to the Schwarzschild metric when $\alpha = 0$ and $\alpha_n = 0$, and to the Kerr metric when $\alpha_n = 0$.

In its most general form, the MN metric is not free from pathologies. This is expected because the only asymptotically flat and stationary BH solution of Einstein's vacuum equations that is non-singular on and outside the event horizon is the Kerr metric (no-hair theorem). In fact, the event horizon of the MN metric lies at $x=1$, and it has (in general) a naked singularity on the equatorial plane (at $x=1,\ y=0$) [13,56]. It is however possible that this curvature singularity will not exist, as it may be covered by the exotic compact object's matter, whose gravitational field will only be described by the MN metric in the exterior.

In this study, we will not consider the MN metric in its general form. Instead, we will focus on the special case of $\alpha_n = 0$ for all $n \neq 2$. This corresponds to Kerr with an additional quadrupole deviation. Accordingly, the nonzero parameters in the MN metric are k, α, and α_2, which are related to the mass M and dimensionless spin parameter χ by

$$k = M\frac{1-\alpha^2}{1+\alpha^2}, \tag{8}$$

$$\alpha = \frac{\sqrt{1-\chi^2}-1}{\chi}, \tag{9}$$

$$\alpha_2 = q\frac{M^3}{k^3}, \tag{10}$$

where q is the anomalous quadrupole moment, given by $q = -(Q-Q_K)/M^3$, with Q and Q_K respectively the MN and Kerr quadrupole moments.

This MN metric is interesting because it allows one to perform null tests of the no-hair theorem, by measuring q. In more detail, $q=0$ corresponds to Kerr, $q>0$ would imply that the compact object under consideration is more oblate than a Kerr BH, while $q<0$ would point at a more prolate object. A statistically significant measurement of a nonzero value of q would signal a violation of the no-hair theorem. Such a use of the MN metric for inference using GWs was proposed, e.g., in [72]. This metric has also been used in studies trying to constrain quadrupole deviations using x-ray observations [12,13].

B. Johannson-Psaltis spacetime

The JP metric [57] is another example of a spacetime that describes parametric deviations from Kerr. This metric originates with the familiar Kerr metric, to which deviations are added that are proportional to

$$h(r,\theta)=\sum_{k=0}^{\infty}\left(\epsilon_{2k}+\epsilon_{2k+1}\frac{Mr}{\Sigma}\right)\left(\frac{M^2}{\Sigma}\right)^k, \tag{11}$$

where $\Sigma=r^2+a^2\cos^2\theta$ and ϵ_k are deviation parameters. It was shown in [57] that asymptotic flatness requires $\epsilon_0=\epsilon_1=0$. In the following, we will consider the special case of $\epsilon_k=0$ for $k>3$. In that case, the deviations from Kerr are proportional to the "quadrupole" term

$$h(r,\theta)=\epsilon_3\frac{M^3 r}{\Sigma^2} \tag{12}$$

and the resulting metric is of the form

$$\begin{aligned}ds^2=&-(1+h(r,\theta))\left(1-\frac{2Mr}{\Sigma}\right)dt^2-\frac{4aMr\sin^2\theta}{\Sigma}(1+h(r,\theta))dtd\phi+\frac{\Sigma(1+h(r,\theta))}{\Delta+h(r,\theta)a^2\sin^2\theta}dr^2\\&+\Sigma d\theta^2+\left\{\sin^2\theta\left(r^2+a^2+\frac{2a^2Mr\sin^2\theta}{\Sigma}\right)+h(r,\theta)\frac{a^2(\Sigma+2Mr)\sin^4\theta}{\Sigma}\right\}d\phi^2,\end{aligned} \tag{13}$$

where $\Delta=r^2-2Mr+a^2$. In the limit $\epsilon_3\to 0$, the JP metric reduces to Kerr. From the asymptotic structure of the metric, it is clear that this JP metric has a quadrupole deviation from Kerr proportional to $\epsilon_3 M^3$ in the Newtonian limit.

As in the case of the MN metric, the properties of the event horizon in the JP metric are quite different from Kerr. For negative values of ϵ_3, the event horizon is always closed. However, for positive values of ϵ_3, for any given value of the spin a there exists a maximum value of ϵ_3 beyond which the event horizon is no longer closed [57]. A "break" in the event horizon appears on the equatorial plane, transforming the central object into a naked singularity. In our analysis, we avoid this kind of pathology by excluding the part of the parameter space that corresponds to the aforementioned singularity.

Since its introduction, the JP metric has seen widespread use in testing GR under various frameworks. The simplicity of the parametrized metric makes it a particularly interesting tool in performing null tests of gravity. It has been used in conjunction with x-ray observations to study accretion disks [64,67]. In the context of the GW ringdown, this metric has been used in [29,68], where the analysis is performed assuming small ϵ_3. Typical values of ϵ_3 that agree with data may be as large as $\sim$14, which casts some doubt on the validity of such an assumption. We avoid these restrictions in our study, and allow ϵ_3 to vary within a wide range while estimating the posterior distribution from data.

III. EIKONAL APPROXIMATION

Given an alternative theory of gravity, the first step toward testing it with ringdown signals is to devise a way to calculate its QNMs. This is not easy to do in arbitrary spacetimes. The usual prescription involves solving the BH perturbation equations under appropriate boundary conditions. On the Kerr spacetime, such equations can be solved by separation of variables, but this is typically not possible on more generic background and/or beyond GR. This calls for alternative formalisms/approximations for calculating QNMs.

Fortunately, QNMs and unstable null geodesics of the background are closely related in the eikonal, or short-wavelength, approximation. The latter was initially investigated by Press [73] (see also Goebel's comment on the same [74]). It has since been understood that the real part of the QNM frequencies in Kerr is related to the frequency of the unstable light ring, and their imaginary part is related to its instability timescale. Ferrari and Mashhoon provided seminal contributions to extending this line of thought [75,76]. In more recent times, this has also been explored in [77–81].

QNMs are indexed by three numbers—n, ℓ and m. n is the overtone number and ℓ and m are the indices of the (ℓ,m) multipole. In the eikonal regime ($\ell,m\gg 1$), the Kerr QNM frequency for the maximally corotating mode $\ell=m$ is

$$\omega_{\rm QNM}=\ell\Omega-i\gamma\left(n+\frac{1}{2}\right), \tag{14}$$

where Ω is the orbital frequency of light rays on the unstable equatorial circular orbit, and γ is the Lyapunov exponent of the same orbit. The Lyapunov exponent characterizes the timescale on which the cross section of a congruence of null rays increases under radial perturbations. Though Eq. (14) is only strictly valid for $\ell,m\gg 1$, it works remarkably well for low values of ℓ as well [82,83].

The eikonal approximation is clearly an incredibly powerful tool, because one only needs to calculate the radius and Lyapunov exponent of the unstable circular equatorial null orbit to calculate the QNM frequencies, without having to solve the BH perturbation equations. In the following, as in Ref. [68], we will make the

physically reasonable (although unproven[2]) assumption that the relation between null orbits and QNM frequencies also holds on (stationary and axisymmetric) backgrounds different from Kerr and in theories beyond GR (see however [85]).

For equatorial null geodesics in a generic stationary and axisymmetric spacetime, one has

$$g_{tt}(u^t)^2 + 2g_{t\varphi}u^t u^\varphi + g_{rr}(u^r)^2 + g_{\varphi\varphi}(u^\varphi)^2 = 0, \quad (15)$$

where $(u^t, u^r, u^\theta, u^\varphi)$ is the four-velocity. From the spacetime symmetries, the conserved quantities are the energy E and angular momentum L, defined by $E = -u_t$ and $L = u_\varphi$. Accordingly, one has

$$u^t = \frac{1}{g_{t\varphi}^2 - g_{tt}g_{\varphi\varphi}}(g_{\varphi\varphi}E + g_{t\varphi}L), \quad (16)$$

and

$$u^\varphi = -\frac{1}{g_{t\varphi}^2 - g_{tt}g_{\varphi\varphi}}(g_{tt}L + g_{t\varphi}E). \quad (17)$$

Using then Eqs. (16) and (17) in Eq. (15), one obtains

$$(u^r)^2 = \frac{1}{g_{rr}(g_{t\varphi}^2 - g_{tt}g_{\varphi\varphi})}(g_{\varphi\varphi}E^2 + 2g_{t\varphi}EL + g_{tt}L^2), \equiv V_{\rm eff}. \quad (18)$$

This equation is of the form $(u^r)^2 = V_{\rm eff}$, where $V_{\rm eff}$ is an effective potential for the radial motion. The turning points of the orbital motion then correspond to locations at which u^r vanishes. In other words, the radial coordinate r_0 at the turning points must satisfy

$$g_{\varphi\varphi}(r_0) + 2g_{t\varphi}(r_0)b + g_{tt}(r_0)b^2 = 0, \quad (19)$$

where $b = L/E$ is the orbit's impact parameter. The angular frequency can then be defined from Eqs. (16) and (17) as $\Omega = u^\varphi/u^t$. Using this in Eq. (15), one has

$$g_{tt}(r_0) + 2g_{t\varphi}(r_0)\Omega_0 + g_{\varphi\varphi}(r_0)\Omega_0^2 = 0, \quad (20)$$

where $\Omega_0 \equiv \Omega(r_0)$. From Eqs. (19) and (20), one finds that at the turning points one has

$$\Omega_0 = 1/b. \quad (21)$$

For circular orbits to exist at $r = r_0$, r_0 must also extremize the effective potential, i.e. r_0 must satisfy the conditions

$$V_{\rm eff}(r_0) = 0 \qquad V'_{\rm eff}(r_0) = 0. \quad (22)$$

Solving these equations, one obtains the radius of the unstable light ring $r_{\rm ph} = r_0$ and the impact parameter b.

Next, let us turn our attention to calculating the Lyapunov exponent, which is related to the decay time of the QNMs. We start with a simple change of radial coordinate, $\mathcal{R} = 1/r$. Eliminating u^r and u^φ from Eqs. (17) and (18), one obtains

$$\left(\frac{d\mathcal{R}}{d\varphi}\right)^2 = \mathcal{R}^4 \frac{(g_{t\varphi}^2 - g_{tt}g_{\varphi\varphi})^2}{(g_{tt}b + g_{t\varphi})^2} V_{\rm eff} \equiv f(\mathcal{R}). \quad (23)$$

For a circular orbit of radius r_0, or equivalently $\mathcal{R}_0 = 1/r_0$, $f(\mathcal{R}) = f'(\mathcal{R}) = 0$. Perturbing the circular null orbit, one can then write

$$\mathcal{R} = \mathcal{R}_0 + \epsilon\mathcal{R}_1 + O(\epsilon^2), \quad (24)$$

where $\epsilon \ll 1$ is a perturbative parameter. It can then be shown [68] that Eq. (23) leads to

$$\frac{d\mathcal{R}_1}{d\varphi} = \pm\kappa_0\mathcal{R}_1, \quad (25)$$

where

$$\kappa_0^2 = \frac{1}{2\mathcal{R}_0^4}f''(\mathcal{R}_0) = \frac{1}{2}\frac{V''_{\rm eff}}{(u^\varphi)^2} \quad (26)$$

is to be evaluated at $r = r_0$. This leads to solutions for $\mathcal{R}_1$ of the form $\mathcal{R}_1 = \mathcal{A}e^{\pm\kappa_0\varphi}$, where $\mathcal{A}$ is a constant. With Ω_0 known, one can write $\varphi = \Omega_0 t + \varphi_0$ where φ_0 is a constant. Using this in Eq. (24), one arrives at

$$\mathcal{R} = \mathcal{R}_0 + \epsilon\mathcal{A}e^{\pm\gamma_0 t}, \quad (27)$$

where

$$\gamma = \kappa_0\Omega_0, = \sqrt{\frac{1}{2}\frac{V''_{\rm eff}}{(u^t)^2}}. \quad (28)$$

To summarize, r_0 and Ω can be found by imposing circular orbit conditions on the effective potential. Subsequently, γ can be calculated at r_0, providing us with all the tools necessary to calculate QNM frequencies with Eq. (14). Although this process is quite straightforward,

[2]Although the correspondence between QNM frequencies and unstable circular orbits is not necessarily automatic beyond GR, it can be proven in some regimes. For instance, if one makes the assumption that the equation for the gravitational perturbations has a principal part given by $\Box h_{\mu\nu}$, where the $\Box$ operator is computed with the modified (e.g. MN or JP) metric, then the correspondence can be established rather rigorously. See, e.g., discussion in Sec. II B of [51] and in Sec. III of [84].

solving the light ring equations can be non-trivial and analytical solutions may not always be possible, in which case one has to resort to numerical solutions.

IV. METHODOLOGY

The GW signal from the ringdown of a binary BH merger can be decomposed into a superposition of damped sines and cosines. If h_+ and $h_\times$ are the two GW polarizations,

$$h_+ - ih_\times = \sum_{\ell m} h_{\ell m}(t)\,{}_{-2}Y_{\ell m}(\iota,\varphi), \tag{29}$$

where ${}_{-2}Y_{\ell m}$ are the spin-weighted spherical harmonics.[3]

The functions $h_{\ell m}(t)$ can be expressed as

$$h_{\ell m}(t) = \sum_n A_{\ell mn} e^{-t/\tau_{\ell mn}} e^{-i\omega_{\ell mn} t + \phi_{\ell mn}}. \tag{30}$$

Here, $A_{\ell mn}$ and $\phi_{\ell mn}$ are the amplitude and phase of the (ℓ, m, n) mode, and $\omega_{\ell mn}$ and $\tau_{\ell mn}$ are its frequency and damping time, respectively.

For quasicircular binary mergers, the dominant mode is $\ell = m = 2$, and in our analysis of GW150914 we restrict ourselves to it. For fixed (ℓ, m), the QNMs can be arranged by their overtone number n, with $n = 0$ being the "fundamental" mode and higher values denoting the "overtones." The question of the detection of overtones in the GW150914 signal is still hotly debated. Although [87,88] claimed a positive detection of the $n = 1$ overtone of the $\ell = m = 2$ mode, subsequent work [36] questioned this claim. In the absence of a consensus on this topic, we shall restrict our analysis of GW150914 to the fundamental mode alone.

The ringdown parameter estimation analysis of GW150914 is obviously accompanied/preceded by the full signal's analysis, which includes the inspiral and merger phases as well. As a result, the sky position, time of merger, and luminosity distance are known quite well. These can then be considered as fixed parameters in the ringdown analysis. The detector measures $h_{\rm strain} = F_+ h_+ + F_\times h_\times$, where F_+ and $F_\times$ are the detector pattern functions, which depend on the right ascension ($= 1.95$ rad), declination ($= -1.27$ rad), polarization ($= 0.82$ rad). Following previous studies on the GW150914 ringdown [36,87], we also fix $(\iota, \varphi) = (\pi, 0)$. For the likelihood computation, we use the time domain method described in [88]. The latter consists of truncating the signal just before the ringdown phase and using the noise covariance matrix to calculate the likelihood in the time domain, without venturing into the frequency domain. This avoids potential data loss due to windowing during fast Fourier transforms. We use the software package RINGDOWN [89] (based on [88]) for data truncation, calculation of the noise covariance matrix and detector pattern functions. We use the publicly available sampler DYNESTY [90], which uses a nested sampling algorithm, to sample the parameter space and calculate the posterior distributions. As for the waveform model, we use the procedure outlined in Sec. III to calculate the QNMs for both metric *ansatze* under consideration. We solve the light ring equations numerically to obtain QNM frequencies as functions of mass, spin and deviation parameter (q for the MN metric and ϵ_3 for the JP metric). The resulting GW strain is then calculated by projecting h_+ and $h_\times$ onto the detector using the pattern functions. We sample the following parameters—remnant mass (M), dimensionless spin (χ), amplitude ($A_{\ell mn}$) and phase ($\phi_{\ell mn}$) of the (ℓ, m, n) mode, along with the deviation parameter (q or ϵ_3). In our analysis of GW150914, we consider only the fundamental $\ell = m = 2$ mode. This means that our model has five free parameters, including q or ϵ_3. Flat priors are assumed on all parameters—$M \in [20, 200] M_\odot$, $\chi \in [0, 0.99]$, $A_{220} \in [0, 5 \times 10^{-20}]$ and $\phi_{220} \in [0, 2\pi]$. As for the deviation parameters, we choose $q \in [-0.16, 0.16]$ and $\epsilon_3 \in [-30, 100]$. As for the data itself, we consider the GW150914 data from both the Hanford and Livingston detectors. We choose the truncation time for the signal from these detectors to be respectively 1126259462.423 s and 1126259462.4160156 s, and a sampling rate of 4096 Hz. The posteriors obtained are presented in Sec V.

V. RESULTS

Let us start by applying the formalism described above to the MN geometry. As is clear from Eqs. (2)–(4), the MN metric is quite involved to work with, and developing BH perturbation theory in such a spacetime is a nontrivial task. In fact, the perturbation equations in general do not separate. This is also the case for many alternative theories of gravity. Fortunately, the procedure outlined in Sec. III is still within reach, and Eq. (22) can indeed be solved.

Starting from the equatorial MN metric, we can easily calculate the effective potential $V_{\rm eff}$ and its radial derivative. We then solve the system (22) numerically to obtain $r_{\rm ph}$ and b as functions of the spin χ and the quadrupole parameter q. The remnant mass enters as a prefactor. We use the data for GW150914, conditioned as described in Sec. IV. The eikonal QNM frequencies are used along with the data to calculate the likelihood for arbitrary values of the sampled parameters—$(M, \chi, A_{220}, \phi_{220}, q)$. As mentioned above, we use DYNESTY and the resulting posterior distributions are shown in Fig. 1. As can be clearly seen, the posterior distribution for q is strongly peaked around zero, which is the Kerr case. This suggests that the Kerr

[3]The ${}_{-2}Y_{\ell m}$ are used as an approximation to the spin-weighted spheroidal harmonics ${}_{-2}S_{\ell m}$, which reduce to ${}_{-2}Y_{\ell m}$ when $a\tilde{\omega}_{lm} = 0$, where $\tilde{\omega}_{lm}$ is the QNM frequency and a is the BH spin. It was however shown that ${}_{-2}S_{\ell m} \approx {}_{-2}Y_{\ell m}$ also for nonzero spins [86].

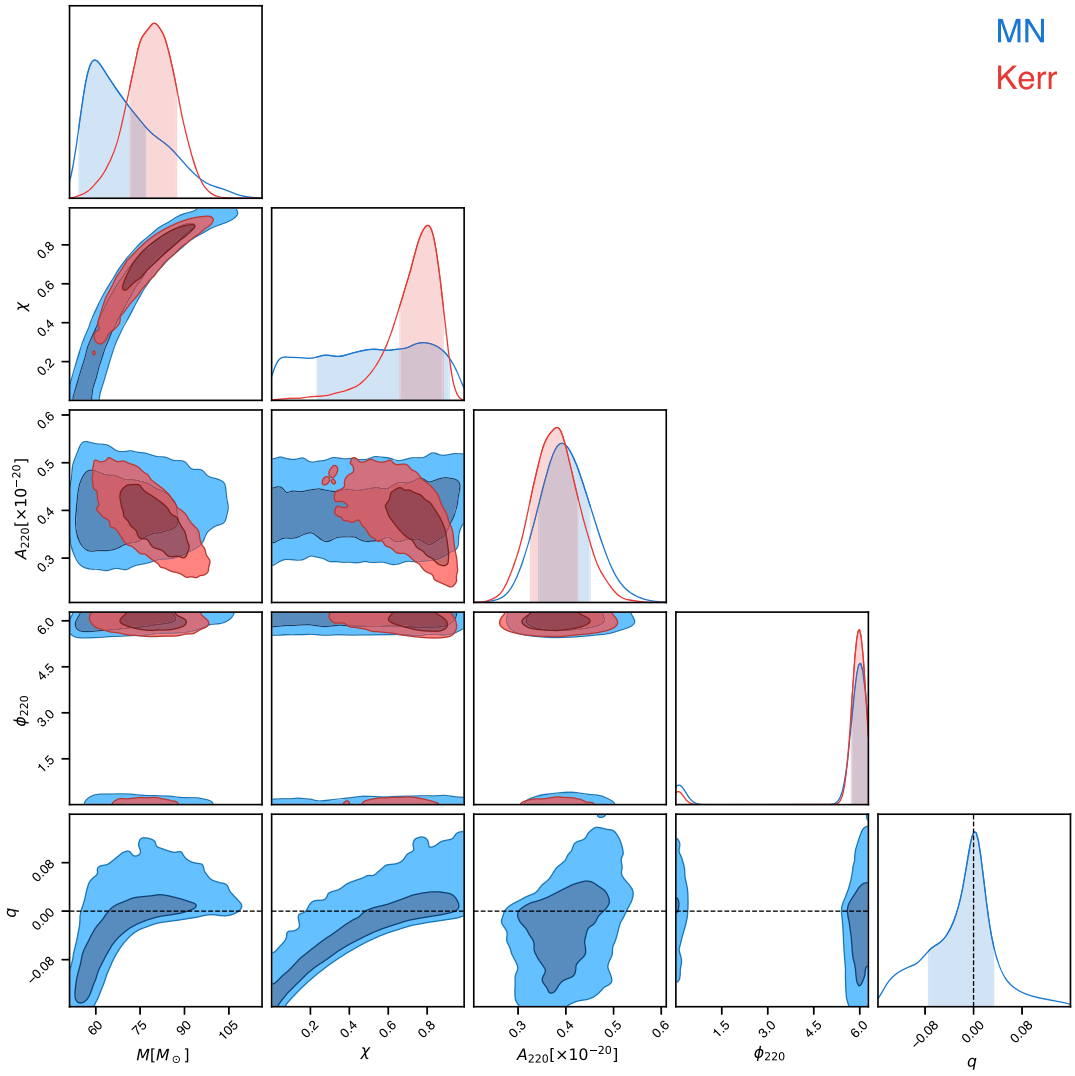

FIG. 1. Posterior distributions for the parameters obtained from the GW150914 data, assuming MN and Kerr background spacetimes. The darker shade in the contours denotes the 1σ confidence level, while the lighter shade denotes the 2σ level. The shaded areas in the one-dimensional histograms correspond to 1σ confidence levels. $q = 0$ (where the MN metric reduces to Kerr) is also highlighted in the distribution with a dotted black line.

hypothesis is indeed favored by the data, although $|q|$ as large as ~ 0.05 are also compatible with the data at 95% confidence level. Another point to note is that the marginalized bounds on χ are uninformative. This is because a change in q can compensate for variations introduced by changes in χ. This is in stark contrast to the Kerr metric, where this degeneracy obviously does not exist and the spin can be bound quite well. It can also be seen that the recovered posterior for M is different from its Kerr counterpart, again due to the degeneracy with q.

The JP metric has been previously used for ringdown analyses [29], but using the Fisher matrix formalism. Moreover, the QNMs were calculated using the prescription described in [68], which involves an expansion in the "small" deviation parameter ϵ_3. However, it is unclear whether this expansion is justified by the data, which may not bound ϵ_3 to a significant degree. In this paper, we use the full form of the JP metric, without imposing any restrictions on the value of ϵ_3, and adopt a Bayesian framework in place of a Fisher matrix one for the estimation of the posterior distributions. Similar to the MN metric case, we use the equatorial JP metric and calculate the QNM frequencies following the procedure outlined in Sec. IV. The estimated posterior distributions are shown in Fig. 2.

While the distribution for ϵ_3 does have a peak near the Kerr value $\epsilon_3 = 0$, it is highly skewed towards $\epsilon_3 > 0$, with virtually no support for negative value. The estimated posteriors for mass M are also quite different from the Kerr and MN ones. In particular, they show support for comparatively larger values of M and smaller values of χ than those predicted for the Kerr metric [87].

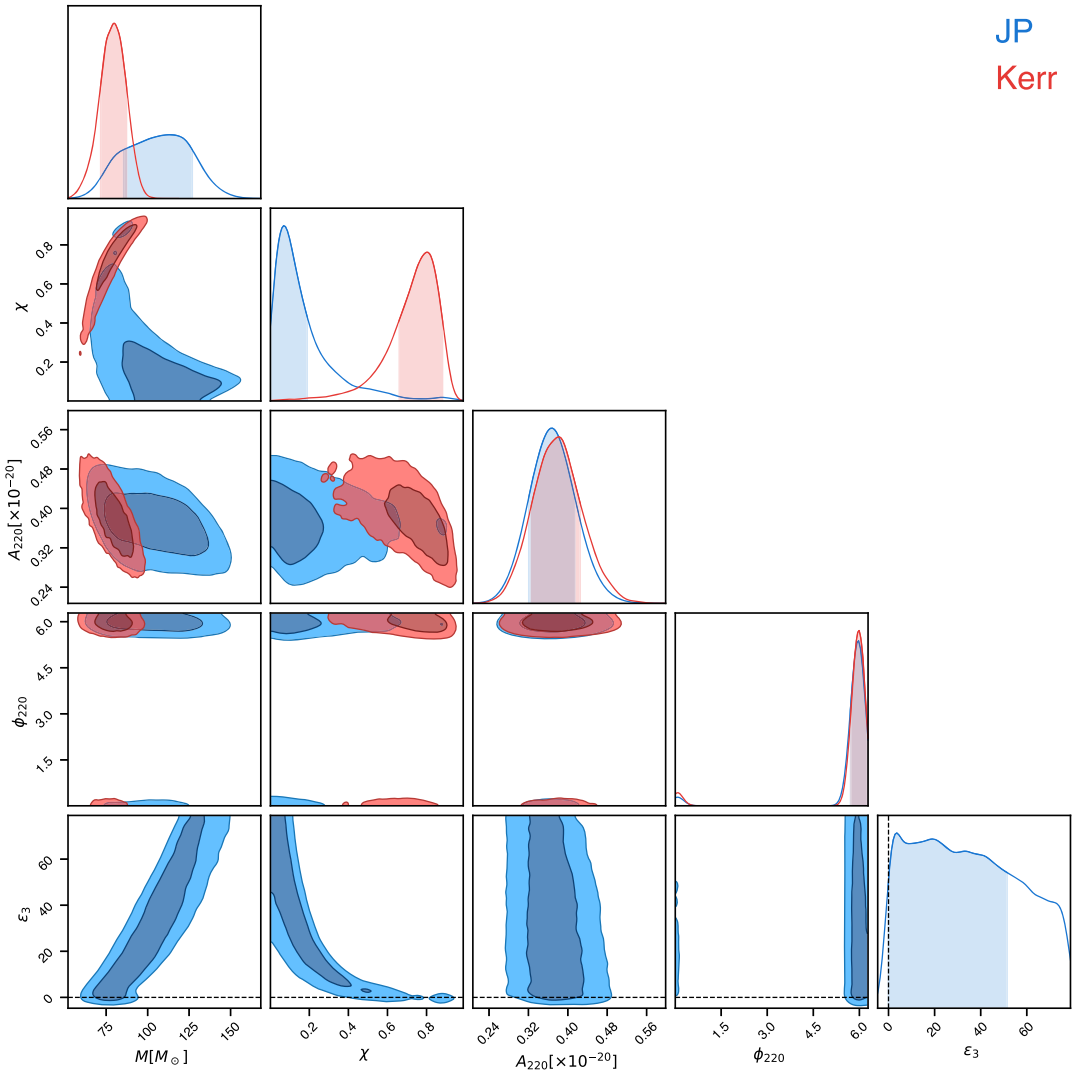

FIG. 2. The same as in Fig. 1, but for the JP spacetime (with large priors on the remnant mass). $\epsilon_3 = 0$ (where the JP metric reduces to Kerr) is also highlighted in the distribution with a dotted black line.

The differences between the posteriors for Kerr and JP are quite striking, especially for χ. This can be understood by examining the analytic form of the QNM frequencies of the JP metric. While such analytic expressions are difficult to compute for arbitrary ϵ_3 [we calculate them by solving Eq. (22) numerically], they can be obtained for small values of ϵ_3. Reference [29] found that for small ϵ_3

$$\omega_{\rm R}^{\rm JP} = \omega_{\rm R}^{\rm K} + \epsilon_3 \left(\frac{1}{81\sqrt{3}M} + \frac{10}{729M}\chi + \frac{47}{1458\sqrt{3}M}\chi^2 \right), \quad (31)$$

$$\omega_{\rm I}^{\rm JP} = \omega_{\rm I}^{\rm K} - \epsilon_3 \left(\frac{1}{486M}\chi + \frac{16}{2187\sqrt{3}M}\chi^2 \right). \quad (32)$$

According to Eq. (31), the effect of the deviation parameter can be countered by smaller values of χ and larger values of M. This is reflected in the posterior distribution for the JP metric, which favors higher M and lower χ compared to Kerr.

Note, however, that the mass of the remnant can be estimated independently from the ringdown and from the inspiral phase. These measurements must of course be consistent [91]. Unfortunately, estimating the mass from the inspiral requires knowledge of the (non-GR) field equations, which do not simply follow from knowledge of the JP geometry. Therefore, performing such a consistency test is not possible in our setting. We can, however, assume that deviations from Kerr and GR are "small", and that the inspiral determination of the mass within GR is approximately correct even if the remnant is described by the JP spacetime (rather than by the Kerr one). Under this assumption, we impose a conservative prior bound on the remnant mass $M \in [55, 100]M_\odot$. (Note that the bound from the inspiral calculated using GR is actually much tighter [92]. We deliberately choose a larger bound to

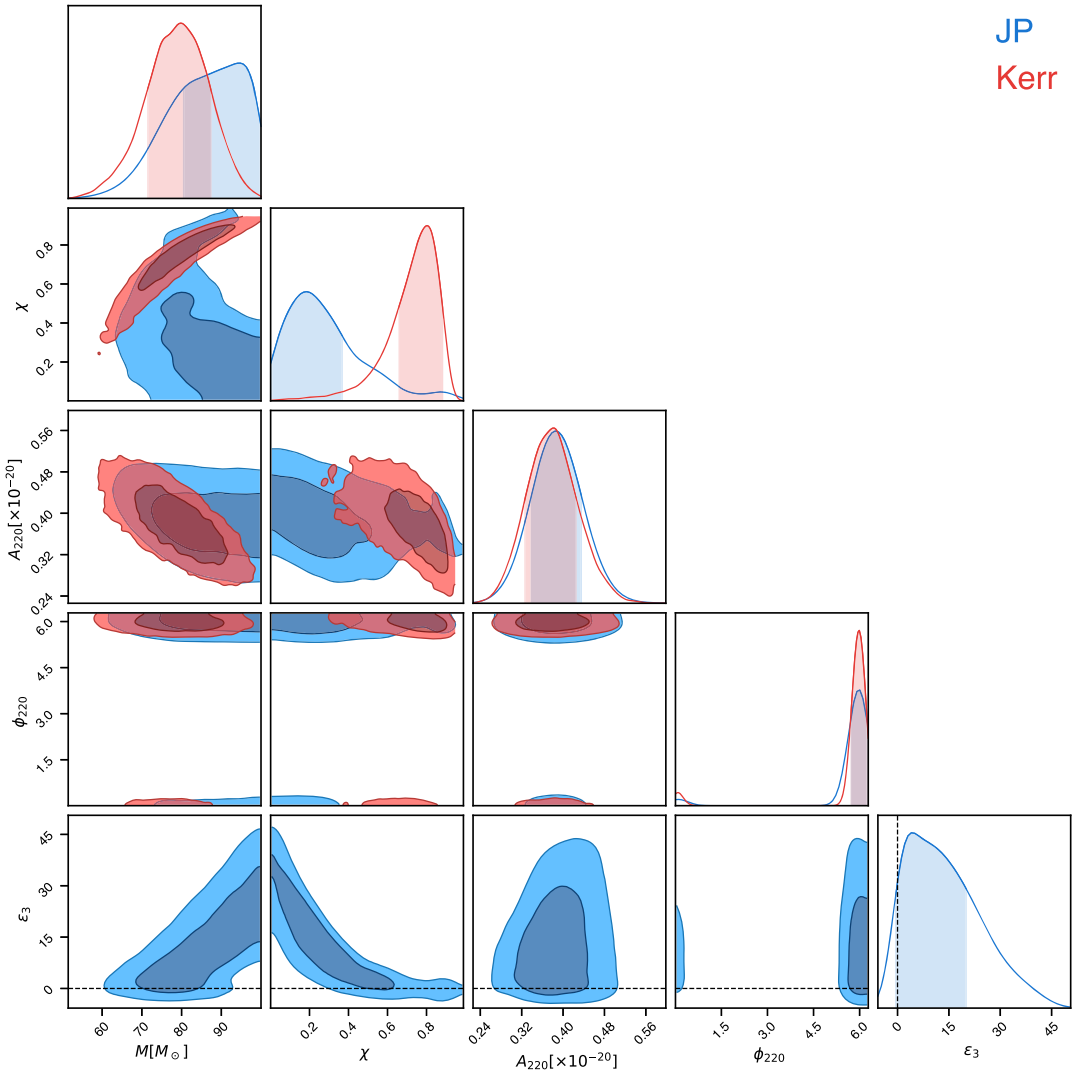

FIG. 3. The same as in Fig. 2, but with a remnant mass prior $M \in [55, 100]M_\odot$.

account for the different remnant geometry.) The resulting posteriors for the JP metric are shown in Fig. 3. While the posteriors for ϵ_3 are still skewed towards positive values, they are now much smaller and consistent with those from [29,64].

We now turn our attention to understanding the asymmetry of the posterior distribution of ϵ_3 about zero. A linear ringdown model of the form of Eq. (30) implies that while performing parameter estimation, the sampler is trying to fit the data to some unknown frequency and damping time along with an amplitude and a phase. The frequency and damping time depend on the remnant mass, spin and deviation parameter. For the GW150914 data, the fitted frequency and damping time lie in the range ~210–240 Hz and ~3–7 ms, respectively. The sampler then searches the parameter space for combinations of mass, spin and deviation parameter that correspond to values in this range. In Fig. 4, we show the dependence of QNM frequency and damping time on spin and ϵ_3, for different values of the remnant mass. The solid black lines denote the portion of the parameter space where the bounds on frequency and damping time are simultaneously satisfied. These lines are not present for low values values of M ($\lesssim 50M_\odot$), because the QNM frequencies are too large and the damping times are too small to agree with the data. As M increases, we start to observe that some points in the parameter space become accessible. For intermediate values of $M < 60M_\odot$, the predicted frequencies lie within the observed bounds for both positive and negative values of ϵ_3, but the bounds on the damping time are satisfied only for positive values (the support for negative values is minimal, as seen in Fig. 4). For higher values of $M > 60M_\odot$, the opposite is true, i.e. the bounds on the damping time are satisfied by a wide range of values of ϵ_3, but the frequency bounds are met mostly for $\epsilon_3 > 0$, with minimal support for negative values. In other words, over a wide range of M, $\epsilon_3 > 0$ leads to frequencies and damping time that simultaneously lie within their respective bounds. This results in $\epsilon_3 > 0$

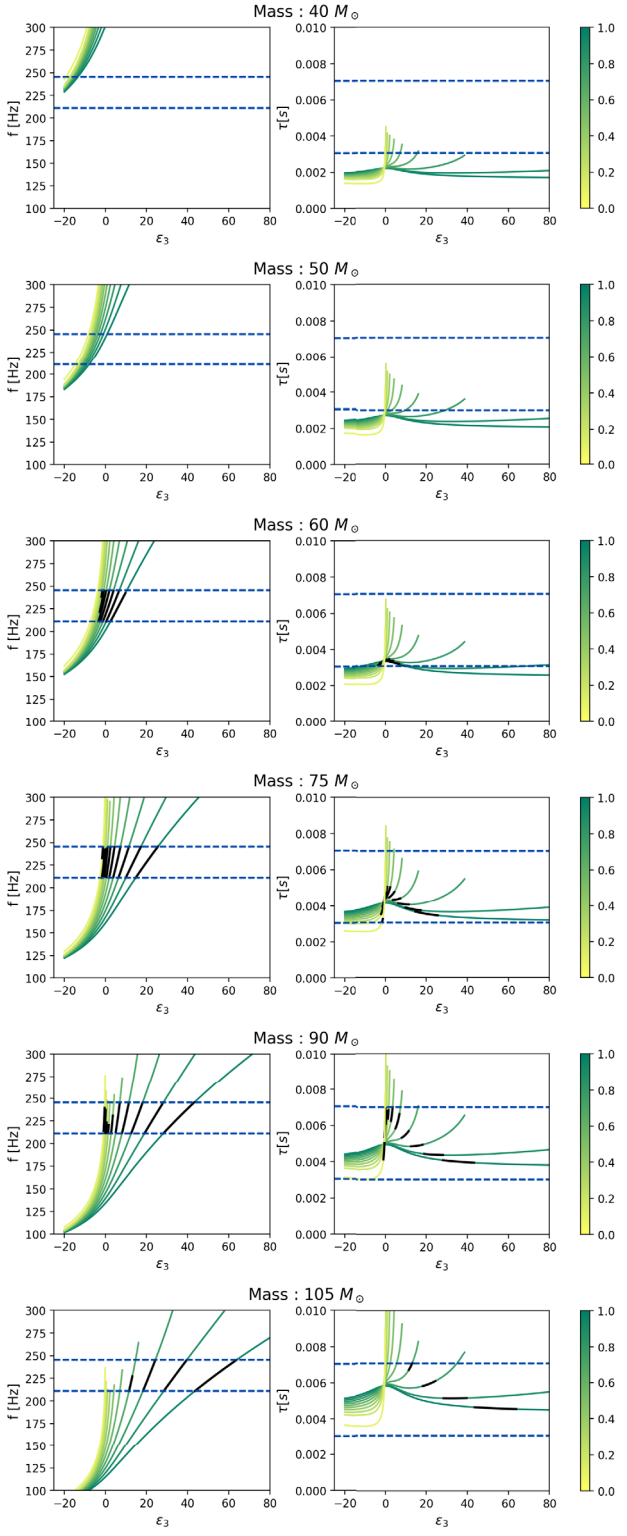

FIG. 4. Dependence of the frequency and damping time of the dominant 220 mode on ϵ_3, for different values of spin and remnant mass. Different spins are denoted by the color axis, which goes from 0 to 1. The blue lines indicate the GW150914 bounds on frequency and damping time. The black lines denote the parameter values for which both bounds are satisfied.

being favored in the posterior distribution shown in Figs. 2 and 3.

With the asymmetry in the posterior distribution of ϵ_3 now understood, we turn our attention to the difference in the estimates of q and ϵ_3. Upon a cursory glance, both denote a quadrupole deviation from Kerr. Multipole moments can be calculated for axisymmetric, asymptotically flat and vacuum spacetimes by performing an asymptotic expansion of the metric functions [93]. This method can be applied to the MN metric and the quadrupole moment $Q_{\rm MN}$ is $Q_{\rm Kerr} - qM^3$. For the JP metric, using a similar asymptotic expansion one finds the quadrupole moment to be $Q_{\rm JP} = Q_{\rm Kerr} + \epsilon_3 M^3$ [68]. The JP metric is, however, not a vacuum spacetime if it is to satisfy the Einstein field equations, which casts doubts on the above result.

Even after restricting the mass priors (in Fig. 3), one can still observe an order of magnitude difference in the posterior bounds on q and ϵ_3. In the eikonal prescription used in this paper, the central quantity of interest is the effective potential $V_{\rm eff}$ defined in Eq. (22). Let us then turn to this potential to understand this discrepancy. Since the MN potential is too cumbersome to work with, we perform an expansion assuming small spin and small quadrupolar deviation (q or ϵ_3).

Solving then Eq. (22) at leading order, the impact parameter is

$$b_{\rm ph}^{\rm MN}/M \approx 3\sqrt{3} - 2\chi + q \tag{33}$$

$$b_{\rm ph}^{\rm JP}/M \approx 3\sqrt{3} - 2\chi - \frac{\epsilon_3}{6\sqrt{3}} \tag{34}$$

in the two geometries. The impact parameter is related to the real part of the QNM frequency through Eqs. (14) and (21). For the two geometries to predict the same QNM frequencies, we must have

$$\epsilon_3 = -6\sqrt{3}q \approx -10q. \tag{35}$$

This relation, however, is not sufficient to explain the posteriors of q and ϵ_3, which differ by a factor $\sim O(100)$. To properly understand this discrepancy, and whether a mapping between the two metrics is even possible at all, we also look at the imaginary part of the QNM frequencies, as given by Eqs. (14) and (28), under the same small parameter expansion. We find

$$\gamma^{\rm MN} \approx \frac{1}{3\sqrt{3}} + \frac{1}{54}(-13 + 12\sqrt{3})q, \tag{36}$$

$$\gamma^{\rm JP} \approx \frac{1}{3\sqrt{3}}. \tag{37}$$

This shows that at the lowest order in spin and deviation parameter, $\gamma^{\rm JP}$ is independent of ϵ_3 whereas $\gamma^{\rm MN}$ depends on q. Therefore, an exact mapping between the parameters q and ϵ_3 does not exist, which explains the different posteriors for the two parameters.

We also calculate $\log_{10}\mathcal{B}^{\rm MN}_{\rm Kerr}$ and $\log_{10}\mathcal{B}^{\rm JP}_{\rm Kerr}$ which are the $\log_{10}$-Bayes factors for the MN and JP metrics compared to Kerr. The value of these factors indicates whether the MN and/or JP hypothesis fits the data better than Kerr. We find $\log_{10}\mathcal{B}^{\rm MN}_{\rm Kerr} = -0.71$ and $\log_{10}\mathcal{B}^{\rm JP}_{\rm Kerr} = -0.25$. The negative values indicate that the Kerr hypothesis is better supported by the GW150914 data.

VI. FUTURE DETECTORS

The LIGO-Virgo-Kagra (LVK) detectors, along with LIGO-India in the coming years, make up the second generation of interferometric GW detectors. These will be followed up by third generation detectors—the Einstein Telescope (ET) [94] and Cosmic Explorer (CE) [95]—and by space based detectors like LISA [10]. These future detectors are designed to allow for lower noise levels, boosting the SNR of detected sources in comparison to LVK. High SNR is an important requirement of ringdown analysis because of the fast decay of QNMs. Indeed low SNRs prevent the use of most GW events for ringdown analyses. GW150914 (and GW190521 [26,96]) is an outlier in this regard. Future detectors are expected to improve on this by providing more eligible sources and higher SNRs [43]. Additionally, higher SNRs will likely lead to detection of higher modes. These modes can also potentially break the degeneracy in M and χ that is observed due to the inclusion of quadrupole deviations in both the MN and JP geometries.

Higher SNR is beneficial for parameter estimation and will lead to an overall shrinkage in the posterior volume. We simulate two different types of signals detectable by ET—one injection containing only the $\ell = m = 2$ mode and one injection containing the $\ell = m = 3$ in addition to the dominant $\ell = m = 2$ mode. The remnant mass and spin of the injected signals are $M = 84M_\odot$ and $\chi = 0.75$, which are similar to GW150914, allowing for a comparison between the posterior bounds across detectors. In order to have a nonzero contribution from the $\ell = m = 3$ mode, we assume $(\iota, \varphi) = (\pi/3, 0)$ [in Eq. (29)] for the injections under consideration. As for the amplitude and phase of the higher mode, we use the fitting formulas provided in [97]. With the $\ell = m = 2$ mode as the reference, the amplitude and phase of the higher mode are redefined as

$$A^R_{330} = \frac{A_{330}}{A_{220}}, \qquad \delta\phi_{330} = \frac{3}{2}\phi_{220} - \phi_{330}. \tag{38}$$

We consider a system where the mass ratio is 3. Using the fitting formulas from [97], we get $A^R_{330} = 0.255$ and $\delta\phi_{330} = 2.95$. The parameters A_{220} and ϕ_{220} are randomly chosen to be 0.44×10^{-20} and 5.37. Moreover, we inject a Kerr signal, with no quadrupole deviations. To this injection, we add simulated noise compatible with the design sensitivity of ET (ET-D sensitivity curve), considering for simplicity a single interferometer in the planned ET "xylophone" configuration [98]. The SNRs of the resulting signals are 176 for the $\ell = m = 2$ only mode, and 179 with the inclusion of the $\ell = m = 3$ mode (as a comparison, the ringdown SNR for GW150914 is ∼13). While sampling, we use the parameters $(M, \chi, A_{220}, A^R_{330}, \phi_{220}, \phi_{330})$, along with the deviation q/ϵ_3 for the MN/JP geometries.

The simulated signal is analyzed according to the process outlined in Sec. IV, with the LIGO detector swapped for ET. We perform this analysis both in the presence and absence of the higher mode for the MN and JP geometries. The results are shown in Figs. 5 and 6, and compared to those obtained with LIGO. The posterior distributions obtained from LIGO GW150914 (in blue) and those from ET (2,2) (in green) are mostly similar, but with a general reduction in the posterior volume. The lower noise levels imply that the QNM frequencies and damping times can be estimated with greater accuracy, but that does not eliminate the degeneracies among M, χ and q (ϵ_3). The decrease in posterior volume in the contours is, on the other hand, quite visible. As for the quadrupolar deviation, the 1σ limits of the posterior distribution decrease by ∼24% for q,

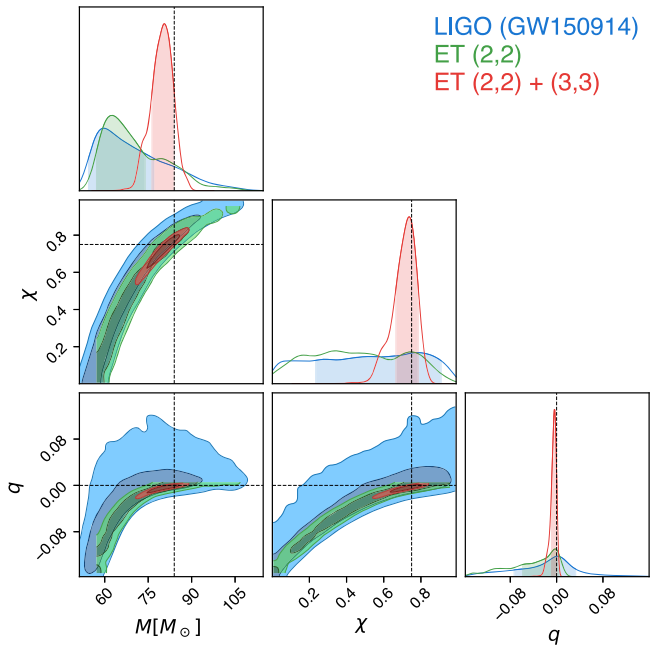

FIG. 5. Posterior distributions for M, χ and q obtained using ET. In red, we show the distributions observed while including the (3,3) mode in addition to the dominant (2,2) mode. The distributions with only the (2,2) mode are shown in green. For reference, the posteriors for GW150914 (which have similar remnant mass and spin) observed with LIGO are shown in blue.

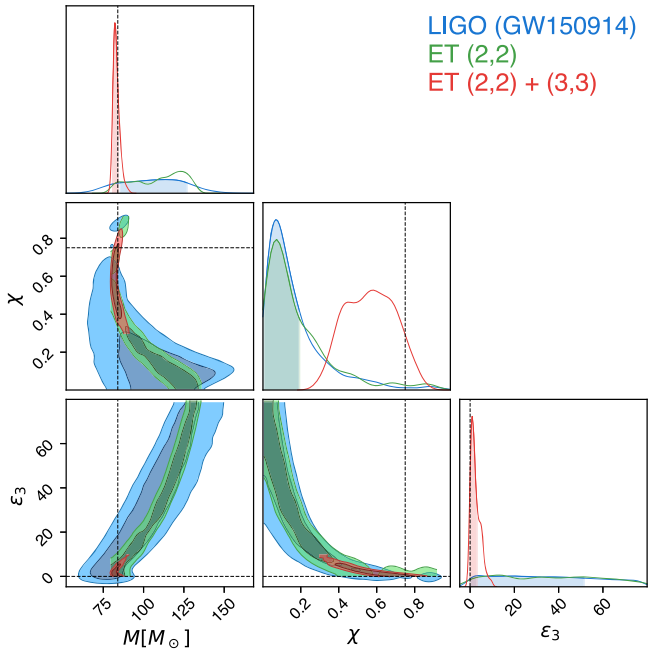

FIG. 6. The same as in Fig. 5, but for the JP case.

while remaining mostly unchanged for ϵ_3, compared to those from LIGO.

Including the $\ell = m = 3$ mode, however, has a much more drastic effect on the posterior distribution. The degeneracy in M, χ and the quadrupole deviation, which is observed in its absence, is no longer seen, and the posterior distributions are mostly peaked around their injected values. In addition, the quadrupole deviation is also much better constrained, with the 1σ limits decreasing by ∼90% for q and ∼94% for ϵ_3, compared to LIGO GW150914. The two-dimensional contours are also constrained much better, signifying a low posterior volume.

VII. CONCLUSION

In this paper, we apply the eikonal approximation to the analysis of real GW data to test the Kerr hypothesis. The ringdown phase of the GW signal contains information about the QNMs emitted by the remnant BH. Measuring these QNMs allows one to gather information about the remnant BH spacetime and the theory of gravity describing BH perturbations. While it has been shown that the final compact object produced by GW150914 is compatible with a Kerr BH, the viability of other alternatives has not been ruled out. We focus here on remnant geometries differing from Kerr as a result of an anomalous quadrupole moment. Its measurement will tell whether the observed data supports the Kerr hypothesis, and whether it is compatible with alternative spacetime geometries as well.

The main difficulty in performing such ringdown analyses is the calculation of the QNM frequencies in an arbitrary axisymmetric and stationary background spacetime. Although this is a non-trivial task, the eikonal approximation allows one to calculate QNM frequencies without having to explicitly solve the BH perturbation equations, by relating the QNM frequencies to the orbital frequency and Lyapunov exponent of the unstable light ring.

We concentrate our efforts on two spacetime metrics for the remnant—the MN and the JP metric. We use restricted versions of these metrics, where deviations from Kerr are regulated by one single parameter, the anomalous quadrupole moment. (We stress that our program can also be applied to remnant geometries whose deviations from Kerr are regulated by two or more parameters.) We use GW150914 data and the eikonal approximation as described in Sec. IV to calculate the posterior distribution for $M, \chi, A_{220}, \phi_{220}$ and the anomalous quadrupole parameter (q or ϵ_3). Our analysis to recover the posterior distributions does not assume deviations from Kerr to be small, and uses full Bayesian methods to calculate the posteriors. The results obtained are shown in Figs. 1 and 2. While the recovered posteriors are compatible with Kerr, for the JP metric *ansatz* the remnant mass is poorly constrained. However, restricting the mass prior by utilizing information from the inspiral-merger analysis, we arrive at bounds on ϵ_3 that are comparable to those from x-ray observations [64,67]. The distribution for ϵ_3 is also quite asymmetric and seems to favor positive values. This can be attributed to the dependence of QNM frequencies and damping time on spin, mass and ϵ_3. We discuss in Sec. V that the frequency and damping times calculated from the sampled parameters must simultaneously satisfy the observational bounds from GW150914, resulting in a skewed distribution. The recovered posteriors for q and ϵ_3 also differ by $\sim O(100)$. As the metrics under consideration are quite involved, we study this feature by assuming a small parameter expansion. We find that the two deviation parameters cannot be mapped to one another, which explains the different width of their posteriors.

We also consider future (third-generation) detectors capable of detecting GW150914-like signals, such as the Einstein Telescope. Starting from simulated injections we recover posterior distributions using the same approach as for GW150914. The posterior distribution covers a smaller volume, but the degeneracies between remnant mass, spin and the anomalous quadrupole remain qualitatively unchanged if one only includes the fundamental mode. However, future detectors will also allow for detecting higher order QNM modes. We find that the inclusion of the (3, 3) mode in the analysis of ET simulated data allows for constraining deviations from the Kerr quadrupole at percent level.

ACKNOWLEDGMENTS

We thank Nicola Franchini, Sebastian H. Völkel and Emanuele Berti for providing useful feedback on the

manuscript. We also thank the referee for useful comments and suggestions. K. D. acknowledges IISER Thiruvananthapuram for providing high-performance computing resources at HPC Padmanabha. E. B. acknowledges support from the European Union's H2020 ERC Consolidator Grant "GRavity from Astrophysical to Microscopic Scales" (Grant No. GRAMS-815673) and the EU Horizon 2020 Research and Innovation Programme under the Marie Sklodowska-Curie Grant Agreement No. 101007855.

[1] R. P. Kerr, Gravitational Field of a Spinning Mass as an Example of Algebraically Special Metrics, Phys. Rev. Lett. **11**, 237 (1963).
[2] E. T. Newman, R. Couch, K. Chinnapared, A. Exton, A. Prakash, and R. Torrence, Metric of a rotating, charged mass, J. Math. Phys. (N.Y.) **6**, 918 (1965).
[3] B. Carter, Global structure of the Kerr family of gravitational fields, Phys. Rev. **174**, 1559 (1968).
[4] D. C. Robinson, Uniqueness of the Kerr Black Hole, Phys. Rev. Lett. **34**, 905 (1975).
[5] E. Barausse, V. Cardoso, and P. Pani, Can environmental effects spoil precision gravitational-wave astrophysics?, Phys. Rev. D **89**, 104059 (2014).
[6] E. Barausse and T. P. Sotiriou, Perturbed Kerr Black Holes Can Probe Deviations from General Relativity, Phys. Rev. Lett. **101**, 099001 (2008).
[7] E. Berti *et al.*, Testing general relativity with present and future astrophysical observations, Classical Quantum Gravity **32**, 243001 (2015).
[8] F. D. Ryan, Gravitational waves from the inspiral of a compact object into a massive, axisymmetric body with arbitrary multipole moments, Phys. Rev. D **52**, 5707 (1995).
[9] F. D. Ryan, Accuracy of estimating the multipole moments of a massive body from the gravitational waves of a binary inspiral, Phys. Rev. D **56**, 1845 (1997).
[10] P. Amaro-Seoane *et al.* (LISA Collaboration), Laser interferometer space antenna, arXiv:1702.00786.
[11] S. Babak, J. Gair, A. Sesana, E. Barausse, C. F. Sopuerta, C. P. L. Berry, E. Berti, P. Amaro-Seoane, A. Petiteau, and A. Klein, Science with the space-based interferometer LISA. V: Extreme mass-ratio inspirals, Phys. Rev. D **95**, 103012 (2017).
[12] C. Bambi and E. Barausse, Constraining the quadrupole moment of stellar-mass black-hole candidates with the continuum fitting method, Astrophys. J. **731**, 121 (2011).
[13] C. Bambi and E. Barausse, The final stages of accretion onto non-Kerr compact objects, Phys. Rev. D **84**, 084034 (2011).
[14] Y. Ni, J. Jiang, and C. Bambi, Testing the Kerr metric with the iron line and the KRZ parametrization, J. Cosmol. Astropart. Phys. 09 (2016) 014.
[15] Y. Dabrowski and A. N. Lasenby, Reflected iron line from a source above a Kerr black hole accretion disc, Mon. Not. R. Astron. Soc. **321**, 605 (2001).
[16] P. Kocherlakota *et al.* (Event Horizon Telescope Collaboration), Constraints on black-hole charges with the 2017 EHT observations of M87*, Phys. Rev. D **103**, 104047 (2021).
[17] K. Akiyama *et al.* (Event Horizon Telescope Collaboration), First Sagittarius A* event horizon telescope results. VI. Testing the black hole metric, Astrophys. J. Lett. **930**, L17 (2022).
[18] B. P. Abbott *et al.* (LIGO Scientific and Virgo Collaborations), Observation of Gravitational Waves from a Binary Black Hole Merger, Phys. Rev. Lett. **116**, 061102 (2016).
[19] B. P. Abbott *et al.* (LIGO Scientific and Virgo Collaborations), GW170104: Observation of a 50-Solar-Mass Binary Black Hole Coalescence at Redshift 0.2, Phys. Rev. Lett. **118**, 221101 (2017); **121**, 129901(E) (2018).
[20] B. P. Abbott *et al.* (LIGO Scientific and Virgo Collaborations), GW170814: A Three-Detector Observation of Gravitational Waves from a Binary Black Hole Coalescence, Phys. Rev. Lett. **119**, 141101 (2017).
[21] B. P. Abbott *et al.* (LIGO Scientific and Virgo Collaborations), GW170817: Observation of Gravitational Waves from a Binary Neutron Star Inspiral, Phys. Rev. Lett. **119**, 161101 (2017).
[22] B. P. Abbott *et al.* (LIGO Scientific and Virgo Collaborations), GW170608: Observation of a 19-solar-mass binary black hole coalescence, Astrophys. J. Lett. **851**, L35 (2017).
[23] B. P. Abbott *et al.* (LIGO Scientific and Virgo Collaborations), GW190425: Observation of a compact binary coalescence with total mass $\sim 3.4 M_{\odot}$, Astrophys. J. Lett. **892**, L3 (2020).
[24] R. Abbott *et al.* (LIGO Scientific and Virgo Collaborations), GW190412: Observation of a binary-black-hole coalescence with asymmetric masses, Phys. Rev. D **102**, 043015 (2020).
[25] R. Abbott *et al.* (LIGO Scientific and Virgo Collaborations), GW190814: Gravitational waves from the coalescence of a 23 solar mass black hole with a 2.6 solar mass compact object, Astrophys. J. Lett. **896**, L44 (2020).
[26] R. Abbott *et al.* (LIGO Scientific and Virgo Collaborations), GW190521: A Binary Black Hole Merger with a Total Mass of $150 M_{\odot}$, Phys. Rev. Lett. **125**, 101102 (2020).
[27] E. Barausse, N. Yunes, and K. Chamberlain, Theory-Agnostic Constraints on Black-Hole Dipole Radiation with Multiband Gravitational-Wave Astrophysics, Phys. Rev. Lett. **116**, 241104 (2016).
[28] A. Cardenas-Avendano, S. Nampalliwar, and N. Yunes, Gravitational-wave versus x-ray tests of strong-field gravity, Classical Quantum Gravity **37**, 135008 (2020).
[29] Z. Carson and K. Yagi, Probing beyond-Kerr spacetimes with inspiral-ringdown corrections to gravitational waves, Phys. Rev. D **101**, 084050 (2020).

[30] B. P. Abbott *et al.* (LIGO Scientific and Virgo Collaborations), Tests of general relativity with the binary black hole signals from the LIGO-Virgo catalog GWTC-1, Phys. Rev. D **100**, 104036 (2019).
[31] R. Abbott *et al.* (LIGO Scientific and Virgo Collaborations), Tests of general relativity with binary black holes from the second LIGO-Virgo gravitational-wave transient catalog, Phys. Rev. D **103**, 122002 (2021).
[32] R. Abbott *et al.* (LIGO Scientific, VIRGO, and KAGRA Collaborations), Tests of general relativity with GWTC-3, arXiv:2112.06861 [Phys. Rev. D (to be published)].
[33] S. Detweiler, Black holes and gravitational waves. III—The resonant frequencies of rotating holes, Astrophys. J. **239**, 292 (1980).
[34] O. Dreyer, B. J. Kelly, B. Krishnan, L. S. Finn, D. Garrison, and R. Lopez-Aleman, Black hole spectroscopy: Testing general relativity through gravitational wave observations, Classical Quantum Gravity **21**, 787 (2004).
[35] E. Berti, V. Cardoso, and C. M. Will, On gravitational-wave spectroscopy of massive black holes with the space interferometer LISA, Phys. Rev. D **73**, 064030 (2006).
[36] R. Cotesta, G. Carullo, E. Berti, and V. Cardoso, Analysis of Ringdown Overtones in GW150914, Phys. Rev. Lett. **129**, 111102 (2022).
[37] E. Finch and C. J. Moore, Searching for a ringdown overtone in GW150914, Phys. Rev. D **106**, 043005 (2022).
[38] M. Isi and W. M. Farr, Revisiting the ringdown of GW150914, arXiv:2202.02941.
[39] C. D. Capano, J. Abedi, S. Kastha, A. H. Nitz, J. Westerweck, Y.-F. Wang, M. Cabero, A. B. Nielsen, and B. Krishnan, Statistical validation of the detection of a subdominant quasi-normal mode in GW190521, arXiv:2209.00640.
[40] L. Sberna, P. Bosch, W. E. East, S. R. Green, and L. Lehner, Nonlinear effects in the black hole ringdown: Absorption-induced mode excitation, Phys. Rev. D **105**, 064046 (2022).
[41] M. H.-Y. Cheung *et al.*, Nonlinear Effects in Black Hole Ringdown, Phys. Rev. Lett. **130**, 081401 (2023).
[42] K. Mitman *et al.*, Nonlinearities in Black Hole Ringdowns, Phys. Rev. Lett. **130**, 081402 (2023).
[43] E. Berti, A. Sesana, E. Barausse, V. Cardoso, and K. Belczynski, Spectroscopy of Kerr Black Holes with Earth- and Space-Based Interferometers, Phys. Rev. Lett. **117**, 101102 (2016).
[44] M. Cabero, J. Westerweck, C. D. Capano, S. Kumar, A. B. Nielsen, and B. Krishnan, Black hole spectroscopy in the next decade, Phys. Rev. D **101**, 064044 (2020).
[45] I. Ota and C. Chirenti, Black hole spectroscopy horizons for current and future gravitational wave detectors, Phys. Rev. D **105**, 044015 (2022).
[46] S. Bhagwat, C. Pacilio, E. Barausse, and P. Pani, Landscape of massive black-hole spectroscopy with LISA and the Einstein Telescope, Phys. Rev. D **105**, 124063 (2022).
[47] J. Meidam, M. Agathos, C. Van Den Broeck, J. Veitch, and B. S. Sathyaprakash, Testing the no-hair theorem with black hole ringdowns using TIGER, Phys. Rev. D **90**, 064009 (2014).
[48] A. Maselli, P. Pani, L. Gualtieri, and E. Berti, Parametrized ringdown spin expansion coefficients: A data-analysis framework for black-hole spectroscopy with multiple events, Phys. Rev. D **101**, 024043 (2020).
[49] V. Cardoso, M. Kimura, A. Maselli, E. Berti, C. F. B. Macedo, and R. McManus, Parametrized black hole quasinormal ringdown: Decoupled equations for nonrotating black holes, Phys. Rev. D **99**, 104077 (2019).
[50] R. McManus, E. Berti, C. F. B. Macedo, M. Kimura, A. Maselli, and V. Cardoso, Parametrized black hole quasinormal ringdown. II. Coupled equations and quadratic corrections for nonrotating black holes, Phys. Rev. D **100**, 044061 (2019).
[51] S. H. Völkel and E. Barausse, Bayesian metric reconstruction with gravitational wave observations, Phys. Rev. D **102**, 084025 (2020).
[52] R. A. Konoplya and A. Zhidenko, First few overtones probe the event horizon geometry, arXiv:2209.00679.
[53] S. H. Völkel, N. Franchini, and E. Barausse, Theory-agnostic reconstruction of potential and couplings from quasinormal modes, Phys. Rev. D **105**, 084046 (2022).
[54] S. H. Völkel, N. Franchini, E. Barausse, and E. Berti, Constraining modifications of black hole perturbation potentials near the light ring with quasinormal modes, Phys. Rev. D **106**, 124036 (2022).
[55] N. Franchini and S. H. Völkel, A parametrized quasi-normal mode framework for non-Schwarzschild metrics, Phys. Rev. D **107**, 124063 (2023).
[56] V. S. Manko and I. D. Novikov, Generalizations of the Kerr and Kerr-Newman metrics possessing an arbitrary set of mass-multipole moments, Classical Quantum Gravity **9**, 2477 (1992).
[57] T. Johannsen and D. Psaltis, Metric for rapidly spinning black holes suitable for strong-field tests of the no-hair theorem, Phys. Rev. D **83**, 124015 (2011).
[58] E. Berti and N. Stergioulas, Approximate matching of analytic and numerical solutions for rapidly rotating neutron stars, Mon. Not. R. Astron. Soc. **350**, 1416 (2004).
[59] L. Rezzolla and A. Zhidenko, New parametrization for spherically symmetric black holes in metric theories of gravity, Phys. Rev. D **90**, 084009 (2014).
[60] R. Konoplya, L. Rezzolla, and A. Zhidenko, General parametrization of axisymmetric black holes in metric theories of gravity, Phys. Rev. D **93**, 064015 (2016).
[61] P. H. C. Siqueira and M. Richartz, Quasinormal modes, quasibound states, scalar clouds, and superradiant instabilities of a Kerr-like black hole, Phys. Rev. D **106**, 024046 (2022).
[62] A. Allahyari, H. Firouzjahi, and B. Mashhoon, Quasinormal modes of generalized black holes: δ-Kerr spacetime, Classical Quantum Gravity **37**, 055006 (2020).
[63] A. Allahyari, H. Firouzjahi, and B. Mashhoon, Quasinormal modes of a black hole with quadrupole moment, Phys. Rev. D **99**, 044005 (2019).
[64] L. Kong, Z. Li, and C. Bambi, Constraints on the spacetime geometry around 10 stellar-mass black hole candidates from the disk's thermal spectrum, Astrophys. J. **797**, 78 (2014).
[65] C. Bambi, Can we constrain the maximum value for the spin parameter of the super-massive objects in galactic nuclei without knowing their actual nature?, Phys. Lett. B **705**, 5 (2011).

[66] C. Bambi, Probing the space-time geometry around black hole candidates with the resonance models for high-frequency QPOs and comparison with the continuum-fitting method, J. Cosmol. Astropart. Phys. 09 (2012) 014.
[67] C. Bambi, J. Jiang, and J. F. Steiner, Testing the no-hair theorem with the continuum-fitting and the iron line methods: A short review, Classical Quantum Gravity **33**, 064001 (2016).
[68] K. Glampedakis, G. Pappas, H. O. Silva, and E. Berti, Post-Kerr black hole spectroscopy, Phys. Rev. D **96**, 064054 (2017).
[69] K. Glampedakis and H. O. Silva, Eikonal quasinormal modes of black holes beyond general relativity, Phys. Rev. D **100**, 044040 (2019).
[70] R. O. Hansen, Multipole moments of stationary space-times, J. Math. Phys. (N.Y.) **15**, 46 (1974).
[71] R. P. Geroch, Multipole moments. II. Curved space, J. Math. Phys. (N.Y.) **11**, 2580 (1970).
[72] J. R. Gair, C. Li, and I. Mandel, Observable properties of orbits in exact bumpy spacetimes, Phys. Rev. D **77**, 024035 (2008).
[73] W. H. Press, Long wave trains of gravitational waves from a vibrating black hole, Astrophys. J. **170**, L105 (1971).
[74] C. J. Goebel, Comments on the "vibrations" of a black hole, Astrophys. J. **172**, L95 (1972).
[75] V. Ferrari and B. Mashhoon, New approach to the quasinormal modes of a black hole, Phys. Rev. D **30**, 295 (1984).
[76] B. Mashhoon, Stability of charged rotating black holes in the eikonal approximation, Phys. Rev. D **31**, 290 (1985).
[77] S. R. Dolan, Quasinormal mode spectrum of a Kerr black hole in the eikonal limit, Phys. Rev. D **82**, 104003 (2010).
[78] H. Yang, D. A. Nichols, F. Zhang, A. Zimmerman, Z. Zhang, and Y. Chen, Quasinormal-mode spectrum of Kerr black holes and its geometric interpretation, Phys. Rev. D **86**, 104006 (2012).
[79] H. Yang, A. Zimmerman, A. Zenginoğlu, F. Zhang, E. Berti, and Y. Chen, Quasinormal modes of nearly extremal Kerr spacetimes: Spectrum bifurcation and power-law ringdown, Phys. Rev. D **88**, 044047 (2013).
[80] H. Yang, F. Zhang, A. Zimmerman, D. A. Nichols, E. Berti, and Y. Chen, Branching of quasinormal modes for nearly extremal Kerr black holes, Phys. Rev. D **87**, 041502 (2013).
[81] V. Cardoso, A. S. Miranda, E. Berti, H. Witek, and V. T. Zanchin, Geodesic stability, Lyapunov exponents and quasinormal modes, Phys. Rev. D **79**, 064016 (2009).
[82] E. Berti and K. D. Kokkotas, Quasinormal modes of Kerr-Newman black holes: Coupling of electromagnetic and gravitational perturbations, Phys. Rev. D **71**, 124008 (2005).
[83] S. Iyer, Black hole normal modes: A WKB approach. 2. Schwarzschild black holes, Phys. Rev. D **35**, 3632 (1987).
[84] R. Ghosh, N. Franchini, S. H. Völkel, and E. Barausse, Quasi-normal modes of non-separable perturbation equations: The scalar non-Kerr case, arXiv:2303.00088.
[85] G. Khanna and R. H. Price, Black hole ringing, quasinormal modes, and light rings, Phys. Rev. D **95**, 081501 (2017).
[86] E. Berti, V. Cardoso, and M. Casals, Eigenvalues and eigenfunctions of spin-weighted spheroidal harmonics in four and higher dimensions, Phys. Rev. D **73**, 024013 (2006); **73**, 109902(E) (2006).
[87] M. Isi, M. Giesler, W. M. Farr, M. A. Scheel, and S. A. Teukolsky, Testing the No-Hair Theorem with GW150914, Phys. Rev. Lett. **123**, 111102 (2019).
[88] M. Isi and W. M. Farr, Analyzing black-hole ringdowns, arXiv:2107.05609.
[89] M. Isi and W. M. Farr, maxisi/ringdown: Initial ringdown release, 10.5281/zenodo.5094068 (2021).
[90] S. Koposov, J. Speagle *et al.*, joshspeagle/dynesty: v1.2.3, 10.5281/zenodo.6609296 (2022).
[91] A. Ghosh *et al.*, Testing general relativity using golden black-hole binaries, Phys. Rev. D **94**, 021101 (2016).
[92] B. P. Abbott *et al.* (LIGO Scientific and Virgo Collaborations), Properties of the Binary Black Hole Merger GW150914, Phys. Rev. Lett. **116**, 241102 (2016).
[93] F. D. Ryan, Spinning boson stars with large self-interaction, Phys. Rev. D **55**, 6081 (1997).
[94] M. Punturo *et al.*, The Einstein Telescope: A third-generation gravitational wave observatory, Classical Quantum Gravity **27**, 194002 (2010).
[95] D. Reitze *et al.*, Cosmic Explorer: The U.S. contribution to gravitational-wave astronomy beyond LIGO, Bull. Am. Astron. Soc. **51**, 035 (2019).
[96] C. D. Capano, M. Cabero, J. Westerweck, J. Abedi, S. Kastha, A. H. Nitz, A. B. Nielsen, and B. Krishnan, Observation of a multimode quasi-normal spectrum from a perturbed black hole, arXiv:2105.05238.
[97] X. J. Forteza, S. Bhagwat, S. Kumar, and P. Pani, Novel Ringdown Amplitude-Phase Consistency Test, Phys. Rev. Lett. **130**, 021001 (2023).
[98] S. Hild *et al.*, Sensitivity studies for third-generation gravitational wave observatories, Classical Quantum Gravity **28**, 094013 (2011).